Interplay between Crystallization and Phase Separation in PS-b-PMMA/PEO Blends: The Effect of Confinement

Article *in* Macromolecules · May 2013

Impact Factor: 5.8 · DOI: 10.1021/ma4005692

3 authors, including:

Xu-Ming Xie
Tsinghua University
179 PUBLICATIONS **1,844** CITATIONS

Macromolecules

Article

pubs.acs.org/Macromolecules

Interplay between Crystallization and Phase Separation in PS-*b*-PMMA/PEO Blends: The Effect of Confinement

Nan Chen, Li-Tang Yan, and Xu-Ming Xie*

Key Laboratory of Advanced Materials (MOE), Department of Chemical Engineering, Tsinghua University, Beijing 100084, China

Supporting Information

ABSTRACT: Interplay between phase separation and crystallization under confinement for the blends of PEO homopolymers with different molecular weight and PS-*b*-PMMA block copolymer is studied. Phase structures of the blends are investigated by atomic force microscope (AFM) and theoretically simulated by the dissipative particle dynamics (DPD) method, and a phase diagram describing the phase structure is established. Low molecular weight PEO (PEO2) disperses uniformly in the PMMA block domain and causes a transition from cylinder phase to perforated lamellar phase, while high molecular weight PEO (PEO20) causes expansion of the cylinder domains and formation of disordered domains. Crystallization and melting behavior of the blends are detected by differential scanning calorimetry (DSC). The results show the liquid−liquid phase separation between PEO homopolymer and PMMA block under PS-*b*-PMMA microphase-separated structure is suppressed due to the hard confinement caused by glassy PS block. As a result, in the blends of PS-*b*-PMMA/PEO2, PEO2 is unable to crystallize, and in the blends of PS-*b*-PMMA/PEO20, PEO20 shows a more obvious melting point depression compared with the homopolymer blends of PMMA/PEO20.

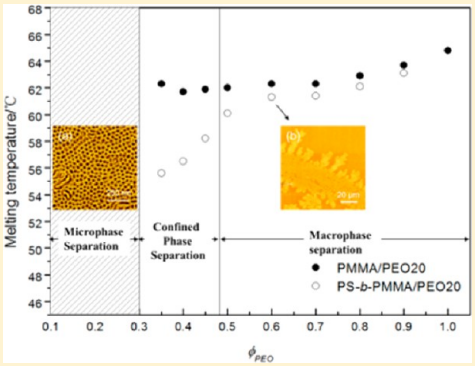

INTRODUCTION

Confinement has very interesting effects on polymer systems with respect to both the crystallization and phase separation of polymers. As the development of nanotechnology, phase transition behavior of such a confined system has become a topic of extensive research. For example, when polymer mixtures are confined in thin film, on one hand, the interplay between wetting and phase separation gives rise to the surface-directed spinodal decomposition (SDSD);[1−3] on the other hand, confinement can also induce miscibility in polymer blends due to entropic inhibition of phase separation into micelles and slowing down of chain diffusions.[4−6]

Besides phase separation, crystallization of polymers under confinement has also drawn much attention. Different approaches have been carried out to create 1D, 2D, and 3D confined environments, including self-assembly of block copolymers[7−20] and homopolymers confined in nanopores.[21−23] It has been found that crystallization of polymers under confinement exhibits lower melting points, different crystallization kinetics, and crystal orientation.[7−23] Although confined crystallization or phase separation has been extensively studied separately, there are few studies on confined systems in which crystallization is coupled with phase separation.

Poly(ethylene oxide) (PEO) and poly(methyl methacrylate) (PMMA) can compose mixtures with phase diagram of upper critical solution temperature (USCT).[24−35] Recently, crystallization and phase separation of this blend system are of particular interest due to its dynamically asymmetric nature caused by the large glass transition temperature (T_g) difference.[30−35] Various crystallization behaviors and morphologies can be observed based on different quench depth and pathways. The crystallization of PEO is frustrated when it couples with a simultaneous viscoelastic phase separation.[30,31]

In this study, we try to further elucidate the confinement effect on this system by blending PEO with a block copolymer, polystyrene-*b*-poly(methyl methacrylate). PS-*b*-PMMA is typical block copolymer and can self-assemble into periodic structures with well-defined size of nanometer scale.[19,36,37] The glassy PS blocks can act as "hard walls" to confine the mixtures of PMMA blocks and PEO homopolymers. Previous studies[15,16,38−42] on such block copolymer/homopolymer (AB/H) system mainly focus on the crystallization behavior, and most studies used homopolymers with repeating units identical to one of the blocks of the block copolymer (AB/H_A system) due to the limited numbers of miscible polymer pairs. Studies on homopolymers that are different from either of the blocks but miscible with only one of the blocks (AB/H_C system) are relatively rare.[16,38] According to previous studies,[19,43−46] the solubility of homopolymer in the microdomains of block copolymer is significantly influenced by the ratio of the molecular weight of homopolymer (M_H) to that of the copolymer block (M_A) miscible with the homopolymer (M_H/M_A): for low M_H/M_A values (<1), the homopolymer may

Received: March 17, 2013
Revised: April 10, 2013
Published: April 22, 2013

   dx.doi.org/10.1021/ma4005692 | Macromolecules 2013, 46, 3544−3553

be uniformly distributed in microdomains; as M_H/M_A increases (~1), the homopolymer will be confined within the microdomains; further increase of M_H/M_A (≫1) will lead to macrophase separation. However, in the AB/H_C system, the situation is more complicated. One issue often being neglected in the previous studies is that the phase separation between homopolymer H_C and A block occurs in a preformed and confined microdomain. Crystallization behavior of homopolymer H_C is closely related to the miscibility between H_C and A block. Hence, for blends of one block copolymer and one crystalline homopolymer, the final phase structure and crystallization behavior are the result of interplay between the following three processes (schematically shown in Figure 1):

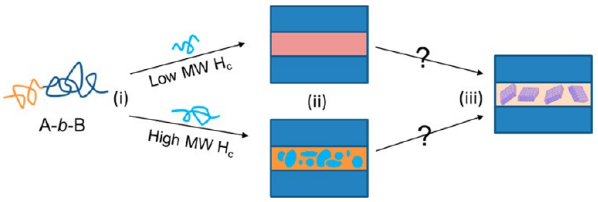

Figure 1. Three possible processes in AB/H_C blends.

(i) microphase separation of the block copolymer AB, producing a confined environment; (ii) liquid–liquid phase separation between the homopolymer H_C and one block under confinement—the phase separation ability can be tuned by changing the molecular weight of H_C; (iii) the crystallization of homopolymer under confinement. It will be very interesting to investigate how these processes interplay with each other. The effect of confinement on liquid–liquid phase separation and crystallization can be studied by comparing the confined system AB/H_C with the unconfined system A/H_C.

EXPERIMENTAL SECTION

Poly(ethylene oxide) samples with different molecular weight (PEO2 (M_n = 2000 g/mol) and PEO20 (M_n = 20 000 g/mol)) were purchased from Aldrich. The asymmetric poly(styrene-*b*-methyl methacrylate) (PS-*b*-PMMA) was purchased from Polymer Source, Inc., with total number-average molecular weight M_n of 77 000 (M_{PS} = 55 000 g/mol and M_{PMMA} = 22 000 g/mol) and polydispersity index M_w/M_n = 1.09. For comparison, an ATRP-synthesized PMMA of almost identical molecular weight (M_n = 20 000 g/mol, PDI = 1.13) with the PMMA block in the PS-*b*-PMMA was used to prepare PMMA/PEO blends.

A predetermined amount of PEO and PS-*b*-PMMA were dissolved in benzene with total polymer concentration of 5 mg/mL and stirred overnight. DSC samples were prepared by direct casting benzene solutions onto a PTFE dish at room temperature. AFM samples were prepared by casting 10 μL solutions on cleaned silicon wafers. The film thickness was determined to be ca. 200 nm by a scratching method on AFM. To remove the residual solvent, the films were dried under vacuum at room temperature for 48 h. In order to compare with PMMA/PEO blends, the weight fraction of PEO in PS-*b*-PMMA/PEO blends is defined as

$$\phi_{PEO} = \frac{m(PEO)}{m(PEO) + m(PMMA\ block)}$$

The corresponding weight fraction of PEO in the whole PS-*b*-PMMA/PEO blends is

$$F_{PEO} = \frac{m(PEO)}{m(PEO) + m(PS\text{-}b\text{-}PMMA)} = \frac{\phi_{PEO}}{\phi_{PEO} + (1 - \phi_{PEO})/(22/77)}$$

The series of PS-*b*-PMMA/PEO blends with different compositions are shown in Table 1.

AFM images were obtained on a SPM-9700, Shimadzu Inc., Japan, in tapping mode. A silicon microcantilever (spring constant 42 N/m and resonance frequency 320 kHz, Nanoworld AG, Switzerland) with a pyramid tip (radius of curvature ~8 nm) was used for scan. The height images and phase images were obtained simultaneously. The operating point ratio (the ratio of operating point amplitude to the free oscillation amplitude) was changed between 0.2 and 0.6 (hard tapping) to acquire the best contrast of phase image.

Differential scanning calorimeter (DSC) measurements were performed on a Shimadzu DSC-60 calibrated with standard indium and zinc, employing a scan rate of 10 °C/min. The X_c of each sample of was calculated by eq 1:

$$X_c = \frac{\Delta H_m}{F_{PEO}\Delta H_m^0} \quad (1)$$

SIMULATION METHODS

To investigate the phase morphology and evolution kinetics of the blends composed of diblock copolymer and homopolymer, a mesoscale method, dissipative particle dynamics (DPD),[47] is used to simulate the blends of diblock copolymer (A_3B_7)/homopolymer (H_p) with various volume fractions and chain lengths of H_p. Corresponding to the experiment, A denotes PMMA block, B denotes PS block, and H_p denotes PEO homopolymers with different molecular weight. DPD is a continuum simulation technique in three dimensions and correctly represents the hydrodynamic interactions. It has been successfully applied to study the mesophase formation of block copolymers with various molecular architectures.[48−50] As a coarse-grained approach, DPD can model physical phenomena occurring at larger time and spatial scales than typical molecular dynamics as it utilizes a momentum-conserving thermostat and soft repulsive interactions between the beads representing clusters of molecules.

In the present simulations, a bead i at position $\mathbf{r}_i$ surrounded by beads $j \neq i$ at $\mathbf{r}_j$ (distance vector $\mathbf{r}_{ij} = \mathbf{r}_i - \mathbf{r}_j$ and unit vector $e_{ij} = \mathbf{r}_{ij}/r_{ij}$ with $r_{ij} = |\mathbf{r}_{ij}|$) experiences a force with the components of conservative interaction force F^C, dissipative force F^D, random force F^R, and bond force F^S, i.e., $f_i = \sum_{j\neq i}(F_{ij}^C + F_{ij}^D + F_{ij}^R + F_{ij}^S)$, where the sum runs over all beads j.[47,48] The conservative force is given by $F_{ij}^C = \alpha_{ij}\omega^C(r_{ij})e_{ij}$, where α_{ij} is the maximum repulsion parameter between beads i and j. The relation between α_{ij} and the Flory–Huggins χ-parameter is given by $\alpha_{ij} \approx \alpha_{ii} + 3.27\chi_{ij}$. Here the interaction parameter between two same bead type α_{ii} is chosen to be 25 in the general DPD simulation. Thus, according to the relative interaction strength between every two species included in the experimental system, we can determine the parameters of α_{ij} used in the simulations. α_{AB} = 40, α_{BH} = 43.3 and α_{AH} = 25.7

Table 1. Composition of PS-*b*-PMMA/PEO Blends

ϕ_{PEO}	1.00	0.90	0.80	0.70	0.60	0.50	0.45	0.40	0.35	0.30
F_{PEO}	1.00	0.72	0.53	0.40	0.30	0.22	0.19	0.16	0.13	0.11

dx.doi.org/10.1021/ma4005692 | Macromolecules 2013, 46, 3544−3553

are set for the other interactions according the real Flory–Huggins parameters of $\chi_{PS-PMMA}$, χ_{PS-PEO}, and $\chi_{PEO-PMMA}$, respectively. The subscripts of A, B denote the beads of each block in the A_3B_7 diblock copolymer and the subscript of H denotes the beads of the homopolymer.[50] Clearly, the A block has strong affinity to the homopolymer while the B block has strong repulsion to the homopolymer. The weight function $\omega^C(r_{ij})$ is chosen as $\omega^C(r_{ij}) = 1 - r_{ij}/r_c$ for $r_{ij} < r_c$ and $\omega^C(r_{ij}) = 0$ for $r_{ij} \geq r_c$, where r_c is the truncate distance. The random force F_{ij}^R and the dissipative force F_{ij}^D are given by $F_{ij}^R = \omega\sigma(r_{ij})\xi_{ij}\Delta t^{-1/2}e_{ij}$ and $F_{ij}^D = -1/2\sigma^2\omega(r_{ij})(v_{ij}\cdot e_{ij})e_{ij}$, where $v_{ij} = v_i - v_j$ and v_i denotes the velocity of bead i. ξ_{ij} is a random number which has zero mean and unit variance. The noise amplitude, σ, which is an inherent parameter of the DPD method, indicates the strength of the noise in the random force and also the strength of the dissipative force. The interaction of these both forces leads to the thermostat of the system. In the general DPD simulation, σ is usually fixed at 3. The bonds between beads in the polymer chain are represented by $F_{ij}^S = Cr_{ij}$ with a stiffness constant $C = -4$. Since the bead–bead interactions in DPD are soft,[51] the crystallization of homopolymer (PEO) will not be simulated. This may lead to some difference between the simulation results and experimental observations of blends with high weight fraction of PEO.

Here we use a modified velocity-Verlet algorithm due to Groot and Warren to solve the motion equation.[47] The radius of interaction, bead mass, and temperature are set as the unit, i.e., $r_c = m = k_BT = 1$. A characteristic time scale is then defined as $\tau = (mr_c^2/k_BT)^{1/2}$. To consider the effects of the ratio between the chain length of the diblock copolymer and that of the homopolymer H_p, the chain length of H_p, p, is increased from 1 to 6. The volume fraction of the homopolymer is also changed so that the total volume fraction of the homopolymer and the A block, ϕ_h, is increased from 0.3 to 0.5, corresponding to the compositions used in the experiments. A 3D box of size of $(20r_c)^3$ is chosen in the simulations, which is large enough to avoid the finite size effects.[49] A bead number density of $3/r_c^3$ is used. The time step of $\Delta t = 0.02\tau$ is chosen, ensuring the accurate temperature control for the simulation systems.[50]

RESULTS AND DISCUSSION

Phase Structure of PS-*b*-PMMA/PEO Blends. Figure 2 shows the AFM height and phase images of a neat PS-*b*-PMMA film. Since the weight fraction of PMMA in the block copolymer is about 30%, a cylindrical microphase separation structure is expected. Figure 3 shows the AFM phase images of thin films of blends of PS-*b*-PMMA with various weight

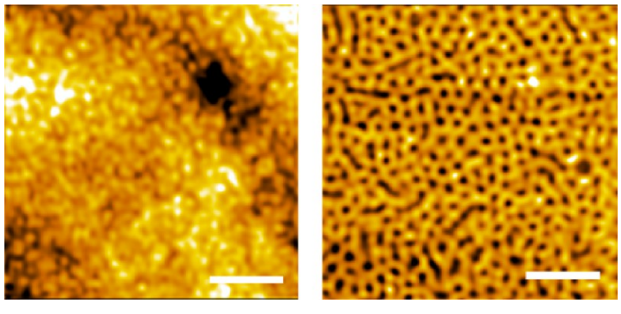

Figure 2. AFM height (left) and phase images (right) of neat PS-*b*-PMMA film. The scale bar is 250 nm.

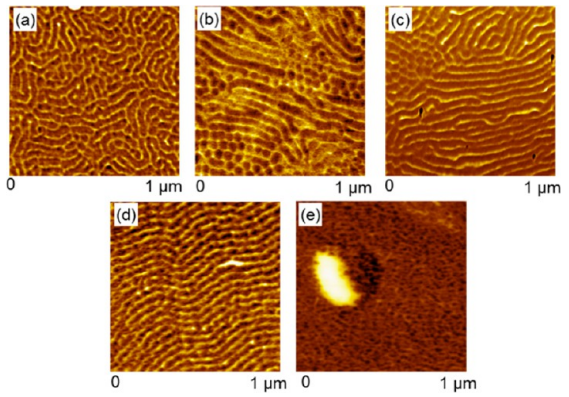

Figure 3. AFM phase images of PS-*b*-PMMA/PEO2 blends with various weight fraction of PEO2 (ϕ_{PEO2}): (a) 0.30, (b) 0.35, (c) 0.40, (d) 0.45, and (e) 0.50.

fractions (ϕ_{PEO2}= 0.3–0.5) of PEO2. Discontinuous and short lamellar microdomains can be observed in the blends of ϕ_{PEO2} = 0.30. As ϕ_{PEO2} increases to 0.35, lamellar microdomains become longer and regular dark dots arranged on the extension line of the lamella can be seen. Similar to previous observations,[52−55] we identify this pattern as a perforated lamella phase. Increasing ϕ_{PEO2} to 0.45 leads to the development of more regular, lamellar microdomains, as shown in Figure 3c,d. Since low molecular weight PEO2 has a good miscibility with the PMMA block, it solubilizes uniformly into the PMMA domains and causes the transition of cylinder phase to lamella phase. Similar evolution of microdomain structure has also been observed in our previous study on the blends of PVCH–PE–PVCH/paraffin[15] systems. At ϕ_{PEO2} = 0.50, bright region with size of several hundred nanometers corresponds to the PEO2 domain, indicating macrophase separation. The dark matrix shows almost disordered microphase structure.

As shown in Figure 4, PS-*b*-PMMA/PEO20 blends present very different phase structure compared to PS-*b*-PMMA/PEO2

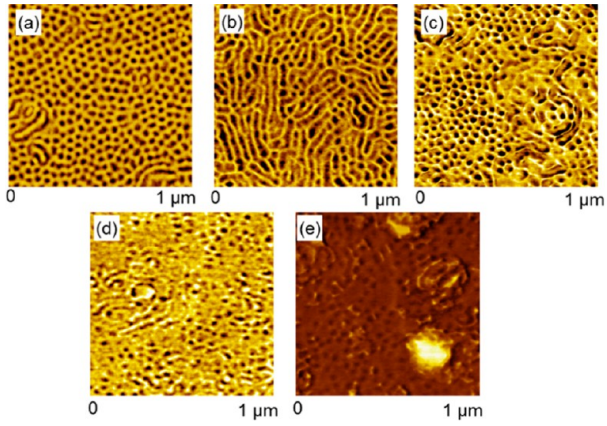

Figure 4. AFM phase images of PS-*b*-PMMA/PEO20 blends with various weight fraction of PEO20 (ϕ_{PEO2}): (a) 0.30, (b) 0.35, (c) 0.40, (d) 0.45, and (e) 0.50.

blends. Blends of ϕ_{PEO20} = 0.30 show regular cylinder microdomains in Figure 4a. Increase of ϕ_{PEO20} to 0.35 leads to expansion and connection of the cylinder domains in Figure 4b. Based on an earlier and systematical study by Russell's group,[19] the expansion of cylinders indicates the localization of high molecular weight homopolymers. At ϕ_{PEO20} = 0.40,

dx.doi.org/10.1021/ma4005692 | Macromolecules 2013, 46, 3544–3553

besides the cylinder domain, some disordered domains are observed, indicating further aggregation of PEO20. More disordered domains are formed at ϕ_{PEO20} = 0.45. When ϕ_{PEO20} reaches 0.50, macrophase separation takes place, which is similar to the situation of PS-*b*-PMMA/PEO2 blends.

Simulation Results for the Phase Morphology and Kinetics of Diblock/Homopolymer Blends. Computer simulations can present the advantage of the morphologies forming spontaneously when started from random configurations and thereby proved a unique approach to explore the mechanism for the phase formation of the systems undergoing microscopic and/or macroscopic phase separation. Although the block copolymer/homopolymer systems have been considered by various simulation techniques,[56,57] there are few studies giving a complete phase diagram for the morphologies of the diblock copolymer/homopolymer systems with various volume fractions and chain lengths of the homopolymer. Herein, we perform a large scale of DPD simulations for the systems composed of A_3B_7 diblock copolymer and homopolymer H_p. The volume fraction and the chain length of the homopolymer are changed in order to examine the influences of these two parameters on the morphologies of the systems and, furthermore, to gain insight into the mechanism of the morphology transition directed by the homopolymer. Although there is no glass transition or the viscoelastic asymmetry in the DPD simulation, it is very powerful in determining the phase morphologies, which have been confirmed in various simulation studies for various polymer systems. Thereby, through the application of DPD simulations, we can determine the phase morphology in a more full view, which greatly facilitates our understanding for the experimental results of the phase morphologies and the crystalline behaviors. Moreover, a phase diagram indicating the relationships of the morphologies and these two parameters is drawn based on the simulation results. It should be pointed out that this phase diagram is obtained based on the dynamical process of the systems instead of the thermodynamically equilibrium calculation. As some structures predicted by the thermodynamic theory cannot or are practically difficult to realize due to the presence of metastable state induced by the energy barrier, the phase diagram based on the dynamical process will facilitate the comparison with the experimental observations. In particular, some new morphologies, e.g., the thick cylinders and the coexistence of disordered phase and cylinders, are identified in the simulations, which will be demonstrated below. Furthermore, the evolution kinetics of systems is also considered in the study, which should provide some useful information for the understanding of the experimental observations.

Figure 5 shows the typical simulated structures of the A_3B_7/H_p polymer blends with the chain length of the homopolymer, p, increasing from 1 to 3. According to Groot et al.'s study,[48] hexagonal cylinders form via a metastable gyroid-like structure and therefore correspond to the nucleation-and-growth mechanism, whereas the lamellar phase is formed via a spinodal decomposition. Although the hexagonal cylindrical structure is definitely demonstrated in Figure 5a, there are still some thin tubes connecting neighboring cylinders. The appearance of the connected tubes indicates that the system gets stuck into a local minimum in free energy surface.[49] A prohibited long time may be needed for the system to jump over this energy barrier.

Figure 5b–e shows the structures of the systems at p = 1, where the total volume fraction of the homopolymer and the A block, ϕ_h, is increased from 0.3 to 0.5 by changing the fraction of the homopolymer. One can find that the cylindrical structure turns to the perforated lamellar structures from ϕ_h = 0.3 to 0.45. At ϕ_h = 0.5, regular lamellae form in the system. Clearly, the structures with all these compositions are ordered at p = 1. The structures of the systems with the same compositions at p = 2 are displayed in Figure 5f–i. In this case, the systems still exhibit perforated lamellae at ϕ_h = 0.3 and 0.35 (see Figure 5f,g). However, the microdomains seem to be more separated compared to the same composition at p = 1 (see Figure 5b,c). At ϕ_h = 0.45, a coexistence of the disordered phase and the cylinders (as marked by the red circle) forms in the system, implying that the ordered structures tends to be destroyed with the further increase of ϕ_h (see Figure 5h). Instead of the formation of the regular lamellae, the structure is absolutely disordered at ϕ_h = 0.5 as shown in Figure 5i. Figure 5j–m presents the structures of the systems with the same compositions at p = 3. At ϕ_h = 0.3, the microdomains keep separating so that the perforated lamellae evolves into hexagonal cylinders (see Figure 5j). However, in contrast to the structures at p = 2, the structures at p = 3 exhibit more disordered from ϕ_h = 0.35. In this case, the appearance of the coexistence of disordered phase and cylinders is advanced to ϕ_h = 0.35 (see Figure 5k). It is interesting that a special mesostructure, characterized by thick, separated, and disordered cylinders, is observed at ϕ_h = 0.45 and p = 3 (see Figure 5l). A similar structure is also observed in other compositions at different homopolymer chain lengths, which can be found in the below phase diagram (Figure 6) of the phase morphology. This structure is different with the absolutely disordered structure as shown in Figure 5m (ϕ_h = 0.5 and p = 3) because the thick cylinders can still be observed although their diameters present large diversity. Actually, the experiment observation demonstrates that the surface roughness (R_a) of ϕ_h = 0.45 is much smaller than that of ϕ_h = 0.5.

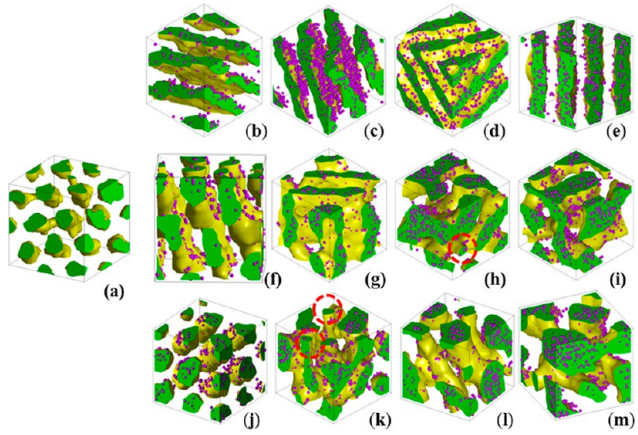

Figure 5. Typical simulated mesostructures in the bulk of the diblock copolymer A_3B_7 without (a) and with homopolymer H_p (b–m). The length of the homopolymer chain, p, of each snapshot is p = 1 (b–e), p = 2 (f–i), and p = 3 (j–m). The total volume fractions of block A and H_p are ϕ_h = 0.3 (b, f, j), ϕ_h = 0.35 (c, g, k), ϕ_h = 0.45 (d, h, l), and ϕ_h = 0.5 (e, i, m). The isosurface of the block copolymer at an order parameter of zero is colored yellow, indicating the interface between block B and other components. The green regions mark phase A and H_p, and the transparent regions indicate phase B. The homopolymers, H_p, are represented by the purple beads. The red circles mark the cylindrical structures in the corresponding snapshots.

dx.doi.org/10.1021/ma4005692 | *Macromolecules* 2013, 46, 3544–3553

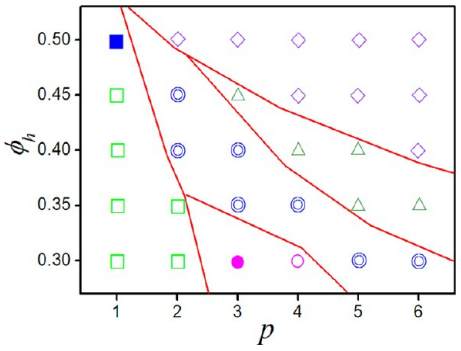

Figure 6. A phase diagram showing the simulated mesostructures of the A_3B_7/H_p blends with various volume fractions ϕ_h and chain lengths p of the homopolymer H_p. The morphologies are (□) perforated lamellae, (■) lamellae, (●) hexagonal cylinders, (○) cylinders, (◎) disordered phase and cylinders, (△) thick cylinders, and (◇) disordered phase. The phase boundary redlines are drawn to guide the eye.

Figure 6 is a phase diagram showing the simulated mesostructures of the A_3B_7/H_p polymer blends in response to various volume fractions and chain lengths of the homopolymer. The phase diagram is obtained based on the dynamical process of the phase evolution instead of the thermodynamically equilibrium theory. Thereby the potential metastable states formed due to the local energy barrier may be included in it, which, however, leads to a better accordance with the experiment observation compared to the phase diagram obtained by the thermodynamically equilibrium calculation. From this phase diagram, one can find that the ordered structures occur in the systems with low volume fraction and short chain length of the homopolymer. Increasing either the volume fraction or the chain length of the homopolymer induces the morphology transition of the blends. We consequently find the formation of ordered structures including perforated lamellae, lamellae, hexagonal cylinders, and cylinders. When the volume fraction and the chain length of the homopolymer are increased to a certain extent, the ordered structures are destroyed. In this case, the phase sections for the coexistence of disordered phase and cylinders, thick cylinders, and disordered phase are present in the phase diagram. By this token, the phase diagram gives a complete view on the morphology transition of the diblock copolymer induced by the homopolymer.

Relatively, the two compositions used in the experiments of the study correspond to the A_3B_7 block copolymer with the homopolymers of H_1 (short polymer chain) and H_3 (long polymer chain or the polymer chain is comparable with the length of the A block), respectively. It also should be pointed out that AFM provides surface information on phase morphology and the DPD simulations give bulk data. The bulk data of the DPD simulations provide a more detailed and clear view on the phase morphology of the blend system, which can help us to understand the experimental results. Basically, the simulated morphologies have a good agreement with those observed in the experiments (see Figures 3 and 4). However, a special case takes place at $\phi_h = 0.5$ and $p = 1$, where a regular lamellar structure is found in the simulation (see Figure 5e), whereas disordered structure is observed in the experiment (see Figure 3e). In this case, the relatively high weight fraction of PEO2 has a strong tendency to crystallize. As mentioned before, DPD methods only predict the phase structure of blends in the amorphous state. In a real experiment, crystallization of PEO2 at high ϕ_{PEO2} value destroys the regular lamellar structure, leading to macrophase separation.

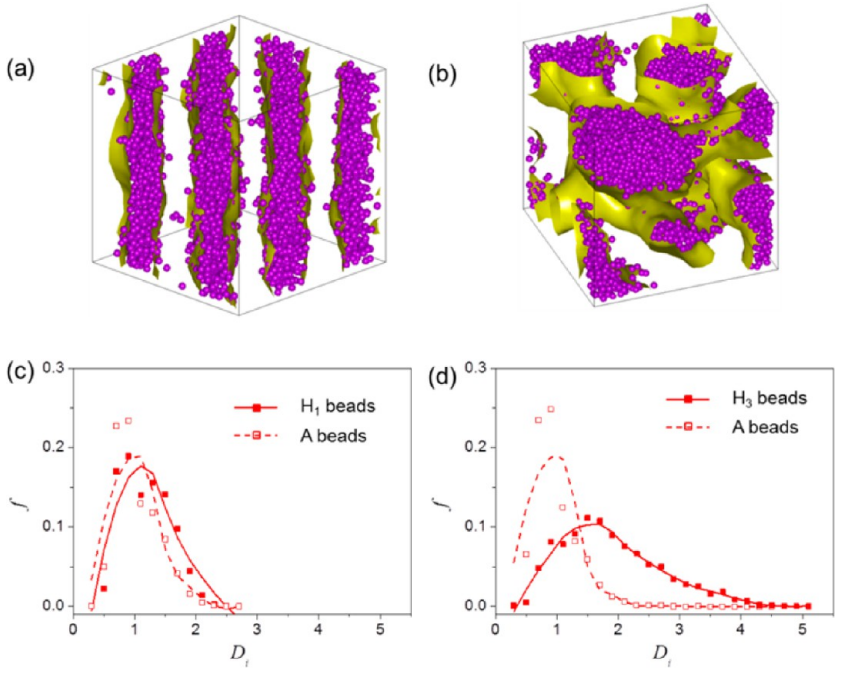

Figure 7. Spatial distribution of homopolymer H_p within the A phase of A_3B_7 diblock copolymers at $\phi_h = 0.5$. (a) $p = 1$ and (b) $p = 3$. These two images correspond to Figures 5e and 5m, respectively. The isosurface of the block copolymer at an order parameter of zero is colored yellow, indicating the interface between block B and other components. The homopolymers, H_p, are represented by the purple beads. DPD beads of A block are not shown here. (c) and (d) show the corresponding statistics of the distance between each H_p bead (or A bead) and the phase interface of block copolymers; the lines are drawn to guide the eye.

dx.doi.org/10.1021/ma4005692 | *Macromolecules* 2013, 46, 3544−3553

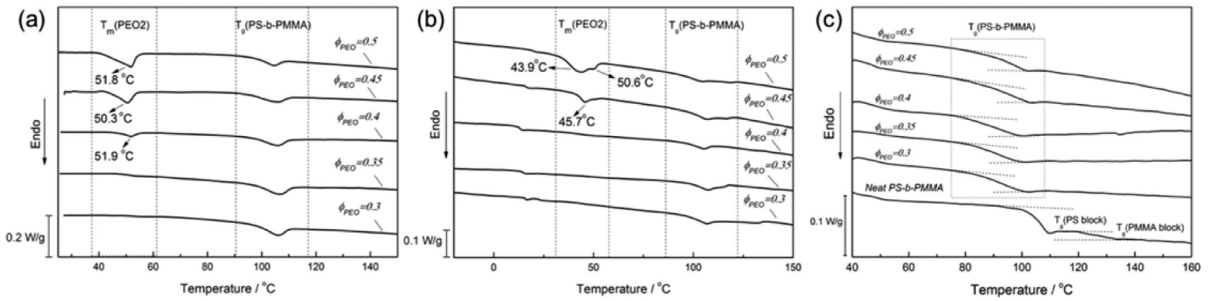

Figure 8. DSC heating curves of PS-*b*-PMMA/PEO2 blends: (a) first heating, (b) after annealing at 180 °C for 1 h, (c) after annealing at 180 °C for 48 h.

To delineate the formation of the various morphologies, we also provide some videos in the Supporting Information, showing the evolution kinetics of the blends with different compositions. The supporting videos 1−4 display the processes of the structure evolution and formation at $\phi_h = 0.3$ and $p = 1$, $\phi_h = 0.4$ and $p = 1$, $\phi_h = 0.3$ and $p = 3$, and $\phi_h = 0.5$ and $p = 3$, respectively. From these videos, we can find that the homopolymer beads gradually move to their preferential phase, although they are randomly dispersed at the initial stage. For the ordered structure, the homopolymer beads present a uniform distribution. However, when the volume fraction and the chain length of the homopolymer are increased to a certain extent, these homopolymer beads will separate from their preferential phase and aggregate at the center of the microdomains, leading to the formation of the macrophase separation. In this case, the defects of the phase are difficult to eliminate, and the ordered structures are destroyed. Obviously, these videos give a clear and detailed description of how the homopolymer beads are included in their preferential domains, how the structure defects of the microdomains are eliminated with the structure evolution, and, finally, how the ordered or the disordered structures form at the final stage.

To gain insight into the mechanism about the morphology transition of the blends composed of diblock copolymer and homopolymer, the spatial distribution of the homopolymer within their preferential microdomains is examined in the study. As an example, Figure 7a,b shows the spatial distribution of the homopolymer beads within phase A, corresponding to the images of Figure 5e,m. As demonstrated in Figures 5e and 7a, the homopolymers with a single bead (H_1) can be uniformly dispersed in their preferential domain. However, at the same concentration of homopolymers, the homopolymers with longer chains (H_3) tend to aggregate and lead to macrophase separation (see Figures 5m and 7b). It should be noted that the total number of the homopolymer beads and the interaction between the homopolymer and the block copolymers are not changed in these two systems. Furthermore, in DPD, the size of the bead representing a fluid unit is also fixed. The only difference is the chain length of the homopolymer, i.e., $p = 1$ in Figure 7a and $p = 3$ in Figure 7b. Thereby, it can be safely concluded that the morphology difference of the two systems is due to the entropy effect because the entropy of the beads linked into a chain (i.e., H_3) is different in both shape and size compared to the single bead (i.e., H_1). We have also quantified the distribution of homopolymer beads within phase domains for these both figures by calculating the distance between each homopolymer bead (or A block bead) and the phase interface of block copolymers. As shown in Figure 7c,d, the distances of all homopolymer beads and A beads to the interface are summarized together, and their distribution in the phase domain can be obtained based on the statistic of the data. Clearly, H_1 almost uniformly distrubute in the A domain while H_3 present a much wider distribution due to their aggregation in the center of A domains with various sizes. The spatial distribution of the inclusions in microdomains of block copolymers is governed by complex interplay between enthalpic and entropic interactions. It should be noted that the homopolymers have a preferential interaction (attraction) with one phase of the block copolymers. This enthalpic interaction tends to constrain the homopolymers in the preferential phase. For the homopolymers with short or long chains, the strengths of enthalpic interaction with block copolymers are not changed. The only change lies at the entropic effect, i.e., the shape and the size of the homopolymers. Thereby, compared to the system with short homopolymer chains, the macrophase separation of the system with long homopolymer chain is induced by the change of the entropic effect. A very initial simulation by Thompson et al.[58] on the basis of mesoscale simulations revealed that larger inclusions localize at the center of their preferential microdomains, whereas smaller nanoparticles are more uniformly dispersed within a specific microdomains. O'Shaughnessy et al.[59] obtained similar conclusions, using analytical scaling theory to investigate the behavior of nanometer-scale inclusions in grafted layers. If the inclusion size is small compared with the contour length of their preferential block, the inclusions are dispersed within this phase, and the overall structures of the nanocomposites are dictated by the block copolymers. However, if the inclusion size is larger compared with the contour length, the polymer must stretch around the inclusions to accommodate them, which will lead to the penalty of the conformation entropy because the extended chains can access fewer conformations than the relaxed coil. When the inclusion size reaches a critical value, this cost in free energy becomes too great, and the inclusions can no longer disperse in their preferential domains; instead, the inclusions are segregated into the center to reduce the stretching of the polymer chains.[58] Although this conclusion was drawn from the block copolymers with nanoparticles, it is still suitable for the understanding of the morphology transition induced by the change of the homopolymer chain length because the radius of gyration of a homopolymer chain is similar to the diameter of a nanoparticle.

Melting Behavior of PS-*b*-PMMA/PEO Blends. The melting and glass transition behavior of PS-*b*-PMMA/PEO2 blends is shown in Figure 8 and Table 2. The first heating curves on DSC reflect the phase separation state of the blends after the solvent evaporation. It should be noted that the phase-separated structure is not in equilibrium, especially for blends

dx.doi.org/10.1021/ma4005692 | *Macromolecules* 2013, 46, 3544−3553

Table 2. Melting Temperature, Crystallinity, and T_g of PS-*b*-PMMA/PEO2 Blends

	ϕ_{PEO2}				
	0.50	0.45	0.40	0.35	0.30
T_m/°C (0 h)	51.8	50.3	51.9		
T_m/°C (1 h)	43.9/50.6	45.7			
T_m/°C (48 h)					
X_c (0 h)	0.07	0.05	0.02		
X_c (1 h)	0.09	0.03			
X_c (48 h)					
T_g[a]/°C (0 h)	96.4	94.2	96.4	97.4	96.9
T_g[a]/°C (1 h)	93.8	95.6	95.4	98.0	96.1
T_g[a]/°C (48 h)	85.2	84.7	80.4	82.1	84.5

[a] T_g data are determined as the onset temperature of glass transition.

with high ϕ_{PEO2}. Blends of ϕ_{PEO2} < 0.40 show no melting peak on the first heating curves in Figure 8a, indicating PEO2 took the amorphous state and dissolved in the PMMA microdomains, which is consistent with the AFM observations (Figure 3a,b) and DPD simulations (Figures 5 and 6). Blends of 0.5 > ϕ_{PEO2} ≥ 0.40 show similar melting points and very low crystallinity (Table 2), indicating most PEO2 are still dissolved in the PMMA microdomain and a small fraction of PEO2 aggregate outside the PMMA domain. This is also supported by the AFM observations of lamellar microphase structure (Figure 3c,d). The blend of ϕ_{PEO2} = 0.50 has a strong tendency to crystallize due to macrophase separation (Figure 3e). After annealing at 180 °C (well above the UCST of PMMA/PEO) for 1 h, PEO2 outside the PMMA lamellar domains gradually migrates into the inside. As a result, the dilute effect becomes pronounced and the melting point depression is about 10 °C (Figure 8b). It should be noticed that the migration and redispersion of PEO2 into the PMMA domains need a certain time to reach equilibrium. This evolution process of phase structure with time can also be observed in the DPD simulation (see Supporting Information). The blends of 1 h annealing time are in an intermediate state. It is also worth to note that in Figure 8c Neat PS-*b*-PMMA shows two T_g on DSC, 103.5 °C for PS block and 120.7 °C for PMMA block, while the blends after 48 h annealing show much lower T_g at 80−85 °C. The depression and broadening of T_g indicate uniform solubilization of PEO2 in the PMMA domain. During the cooling process from 180 to −80 °C, the glass transition of the PS block occurs first, and local segregation of PEO2 inside the PMMA domain is prohibited due to the confinement from the glassy PS block. The absence of the PEO-rich phase frustrates the crystallization of PEO2, so the blends of 48 h annealing time shows no melting peak. The confinement effect of PS block can be further illustrated by a comparison experiment of PMMA/PEO2 blends. As shown in Figure 9, under the same annealing and crystallization conditions, homopolymer blends of PMMA/PEO2, which are free of confinement, can still crystallize.

Increasing the molecular weight of PEO can usually lead to a stronger tendency of liquid−liquid phase separation between PEO and PMMA (or PMMA block). In order to further clarify the effect of confinement on the liquid−liquid phase separation of PMMA/PEO, PEO with higher MW (PEO20) was blended with PS-*b*-PMMA and homo-PMMA, respectively. Taking ϕ_{PEO20} = 0.4 as an example, Figure 10 shows similar depression of crystallinity and melting point. It should also be noted here that the movement of block copolymer is frozen as the solvent evaporates. Thereby, annealing treatment is necessary to get the

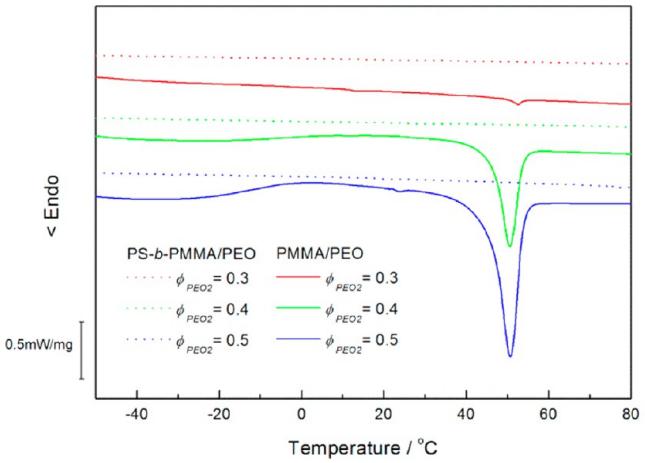

Figure 9. DSC heating curves of PEO2 blended with PS-*b*-PMMA (dotted lines) and homo-PMMA (solid lines).

equilibrium phase structure. However, it takes much more time for PEO20 to completely dissolve in the PMMA domain compared to PEO2 (T_m peak of ϕ_{PEO2} = 0.4 disappears after annealing for only 1 h). The double endotherm peak of PS-*b*-PMMA/PEO20 indicates PEO crystals under two situations. One is crystallized inside the cylinder which is diluted by more fractions of PMMA, resulting in a lower T_m according to Nishi−Wang's equation.[60,61] The other is crystallized outside the cylinder, which exhibits a higher T_m. Annealing leads to more PEO molecules migrating into the PMMA cylindrical domains, which results in the decrease of melting point and crystallinity with annealing time.

Figure 11 shows the DSC curves of one annealed sample (ϕ_{PEO20} = 0.4, annealing time = 4 h) heating from different starting temperature. The upper limit of the heating program was set at 90 °C, which is below the T_g of PS block; therefore, the microphase separation structure will be retained during the heating−cooling circles. The blends show double endotherm peak on the first heating curve: one at 53.4 °C and the other at 57.9 °C. When heated from 20 °C (second heating), the lower T_m disappears while the higher one is retained. When heating from −80 °C again (third heating), the lower T_m occurs again. These results indicate the supercooling needed for the crystallization of PEO inside or outside the cylinder domains are different. The PEO confined in the cylinders needs larger supercooling to induce homogeneous nucleation.[10,23] The results can also be reproduced even during more circles of heating and cooling, with T_m and heat of fusion almost unchanged, as long as the heating upper limit is not beyond 90 °C. This indicates the migration of PEO molecules from disorder domains outside the cylinder into the cylinder is obstructed by the glassy "PS walls". However, once the blends are heated above the T_g of PS block, PEO can migrate into the cylinder. For example, as the annealing time at 180 °C increases to 6 h (Figure 10a), the higher T_m almost disappears while the lower T_m still exists. As mentioned above, PEO20 has a stronger tendency to phase-separate from PMMA compared to PEO2. According to the AFM and DPD results (Figures 4 and 5), PEO20 tends to aggregate in the cylindrical domains, which provides a PEO-rich domain for PEO20 to crystallize. Further increasing the annealing time to 48 h, similar to the situation of PEO2, the T_m peaks completely disappear (Figure 10a). However, if the samples were submitted to isothermal crystallization for a sufficient time (48 h), PEO20 can crystallize

dx.doi.org/10.1021/ma4005692 | Macromolecules 2013, 46, 3544−3553

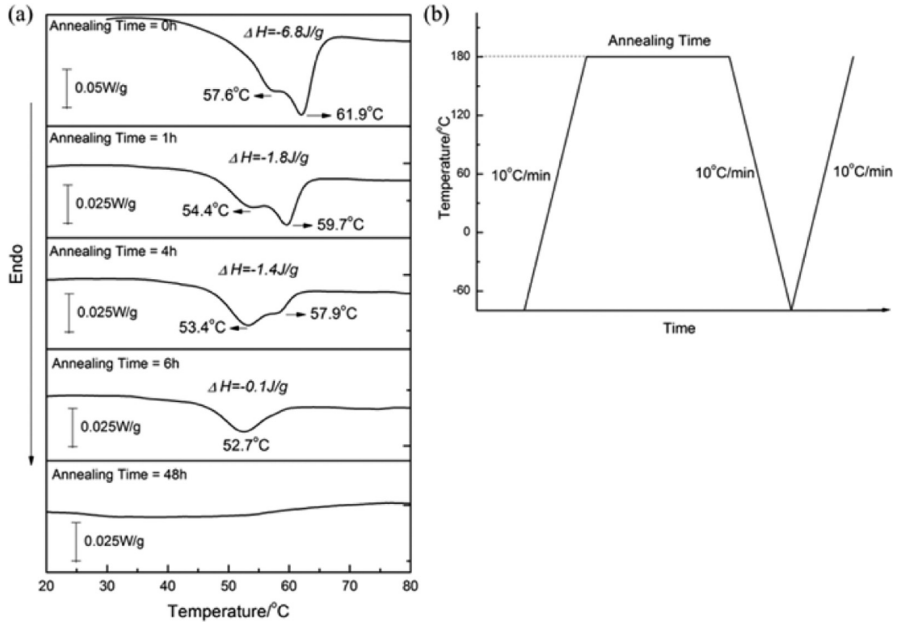

Figure 10. (a) DSC second heating curves of PS-*b*-PMMA/PEO20 blends (ϕ_{PEO20} = 0.4) with different annealing time. (b) Corresponding heating program.

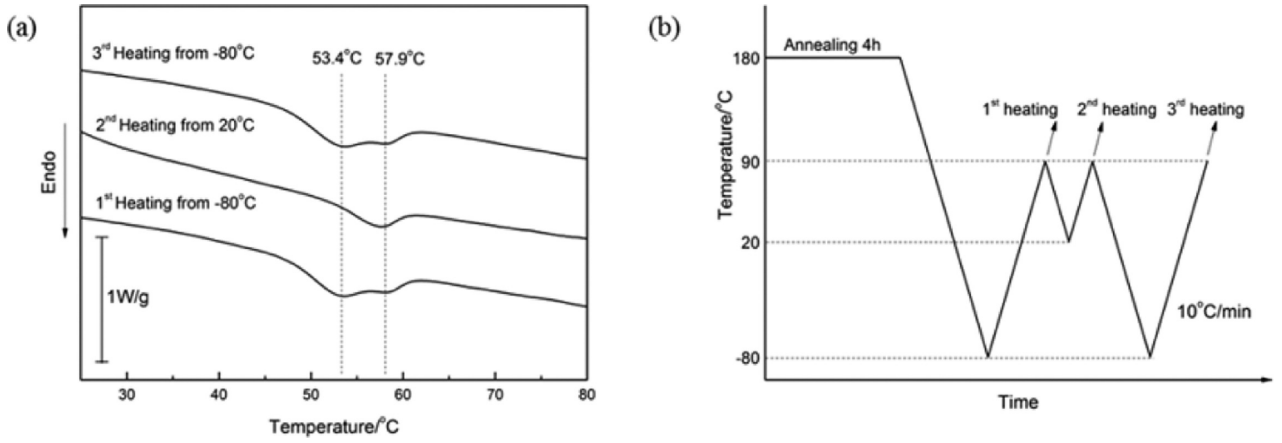

Figure 11. (a) DSC heating curves of PS-*b*-PMMA/PEO20 blends (ϕ_{PEO20} = 0.4, annealing time = 4 h) from different starting temperature. (b) Corresponding heating program.

again, while PEO2 still cannot crystallize. The results are shown in Figure 12.

PS-*b*-PMMA/PEO20 blends with various ϕ_{PEO20} (0.3−0.9) were then submitted to isothermal crystallization at 30 °C for 48 h, and the corresponding T_m are shown in Figure 12 (hollow circles). For comparison, the T_m of homopolymer blends (PMMA/PEO20) are also presented (solid circles). At $\phi_{PEO20} \leq 0.30$, both PS-*b*-PMMA/PEO20 and PMMA/PEO20 show no traces of crystallization; the phase morphology of PS-*b*-PMMA/PEO20 is dominated by cylindrical structure (Figure 12, inset a). At $\phi_{PEO20} > 0.5$, these two series of blends show similar melting point depression. In this range, macrophase separation in PS-*b*-PMMA/PEO20 takes place, and the crystallization of PEO20 breaks through the confinement; take ϕ_{PEO20} = 0.6 as an example, typical dendritic crystals of PEO20 can be observed on AFM (Figure 12, inset b). At $0.30 < \phi_{PEO20} < 0.5$, the T_m of PMMA/PEO20 are almost constant (ca. 62 °C); however, the T_m of PS-*b*-PMMA/PEO20 blends continues to decrease with the decrease of ϕ_{PEO20}.

According to the study by Li et al.[25] in 1984 and recent studies by Han's group[30−33] on PMMA/PEO blends, crystallization of PEO is accompanied by the liquid−liquid phase separation between PEO and PMMA. A PEO-rich phase generated from liquid−liquid phase separation is required for crystallization, and crystallization of PEO can also influence the phase separation in reverse. According to the phase diagram given by Shi et al.,[33] in the region of low PEO weight fraction, crystallization kinetics is greatly depressed; thus, the liquid−liquid phase separation may occur prior to crystallization. This explains the disappearance of melting point depression of PMMA/PEO20 at $0.30 < \phi_{PEO20} < 0.50$. As for the PS-*b*-PMMA/PEO20 blends, however, the liquid−liquid phase separation of PEO and PMMA block is confined in the preformed microdomains. The movement of PMMA blocks is confined by glassy PS blocks; therefore, the liquid−liquid separation generates PEO-rich phases containing a considerable amount of PMMA blocks. In other words, the dilute effect of PMMA on the melting of PEO crystal under confinement is

dx.doi.org/10.1021/ma4005692 | *Macromolecules* 2013, 46, 3544−3553

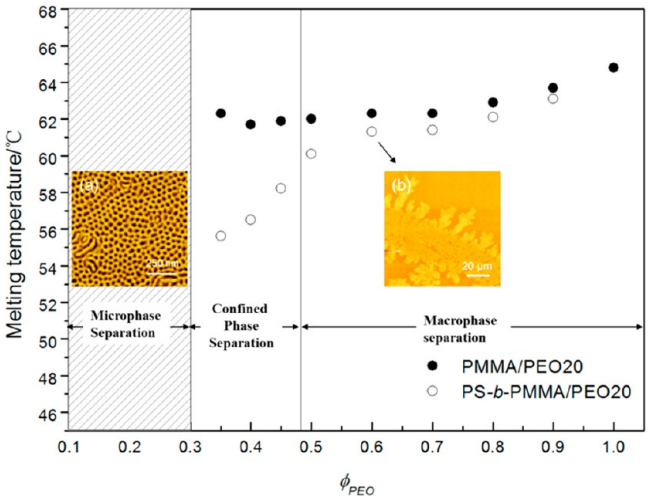

Figure 12. Comparison of melting point depression in PS-*b*-PMMA/PEO20 blends and PMMA/PEO20 blends.

intensified. This confined phase separation and crystallization process is sketched in Figure 13.

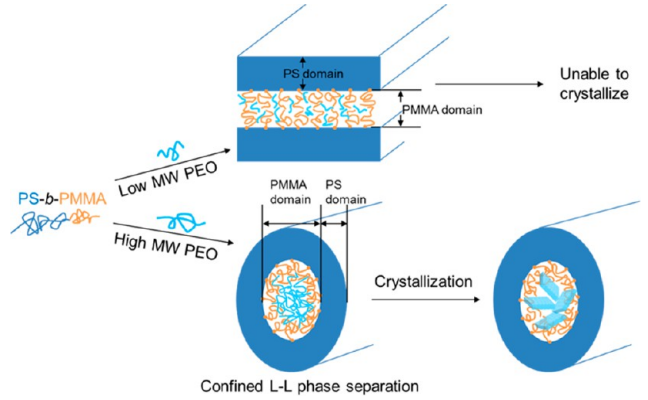

Figure 13. Schema of confined phase separation and crystallization in PS-*b*-PMMA/PEO blends.

CONCLUSION

This work studied the interplay between crystallization and phase separation in the blends of PS-*b*-PMMA/PEO. At ϕ_{PEO2}< 0.5, low molecular weight PEO (PEO2) dissolves uniformly in PMMA microdomains, causing a transition of microphase separation structure from cylinders to perforated lamellas and further to lamellas with increasing PEO weight fraction, while high molecular weight PEO (PEO20) aggregates at the center of cylindrical domains, causing an expansion of cylinder and further formation of disorder domains with increasing PEO weight fraction. DPD simulation provides a phase diagram that helps better understanding the influences of molecular weight and weight fraction of homopolymer on the phase structure of block copolymer/homopolymer blends.

In the blends of PS-*b*-PMMA/PEO, the liquid−liquid phase separation between PEO and PMMA block is confined by the glassy PS block. As a result, low MW PEO (PEO2) is unable to crystallize due to the complete suppression of liquid−liquid phase separation; high MW PEO (PEO20) has a stronger phase-separation ability and can still crystallize. Because of confinement, PS-*b*-PMMA/PEO20 shows more obvious melting point depression compared with PMMA/PEO20.

ASSOCIATED CONTENT

Supporting Information

Videos showing the processes of the structure evolution and formation simulated by the DPD method. This material is available free of charge via the Internet at http://pubs.acs.org.

AUTHOR INFORMATION

Corresponding Author

*E-mail: xxm-dce@mail.tsinghua.edu.cn.

Notes

The authors declare no competing financial interest.

ACKNOWLEDGMENTS

This work is supported by National Natural Science Foundation of China (No. 20874056).

REFERENCES

(1) Binder, K.; Puri, S.; Das, S. K.; Horbach, J. *J. Stat. Phys.* **2010**, *138*, 51−84.
(2) Yan, L. T.; Li, J. L.; Li, Y.; Xie, X. M. *Macromolecules* **2008**, *41*, 3605−3612.
(3) Yan, L. T.; Xie, X. M. *J. Chem. Phys.* **2007**, *126*, 064908.
(4) Hsu, W. P. *Colloids Surf., A* **2010**, *367*, 161−166.
(5) Jiang, K.; Su, Y.; Xie, B.; Meng, Y.; Wang, D. *J. Phys. Chem. B* **2009**, *113*, 3269−3272.
(6) Zhu, S.; Liu, Y.; Rafailovich, M. H.; Sokolov, J.; Gersappe, D.; Winesett, D. A.; Ade, H. *Nature* **1999**, *400*, 49−51.
(7) Cheng, S. Z. D.; Hsiao, M. S.; Zheng, J. X.; Horn, R. M. V.; Quirk, R. P.; Thomas, E. L.; Chen, H. L.; Lotz, B. *Macromolecules* **2009**, *42*, 8343−8352.
(8) Hsiao, M. S.; Chen, W. Y.; Zheng, J. X.; Van Horn, R. M.; Quirk, R. P.; Ivanov, D. A.; Thomas, E. L.; Lotz, B.; Cheng, S. Z. D. *Macromolecules* **2008**, *41*, 4794−4801.
(9) Nojima, S.; Ohguma, Y.; Kadena, K.-i.; Ishizone, T.; Iwasaki, Y.; Yamaguchi, K. *Macromolecules* **2010**, *43*, 3916−3923.
(10) Nojima, S.; Ohguma, Y.; Namiki, S.; Ishizone, T.; Yamaguchi, K. *Macromolecules* **2008**, *41*, 1915−1918.
(11) Sun, Y. S.; Chung, T. M.; Li, Y. J.; Ho, R. M.; Ko, B. T.; Jeng, U. S.; Lotz, B. *Macromolecules* **2006**, *39*, 5782−5788.
(12) Yu, P. Q.; Xie, X. M.; Wang, T.; Bates, F. S. *J. Appl. Polym. Sci.* **2006**, *102*, 2584−2589.
(13) Yu, P. Q.; Xie, X. M.; Wang, Z.; Li, H. S.; Bates, F. S. *Polymer* **2006**, *47*, 1460−1464.
(14) Chen, Y. F.; Zhang, F. B.; Xie, X. M.; Yuan, J. Y. *Polymer* **2007**, *48*, 2755−2761.
(15) Yu, P. Q.; Yan, L. T.; Chen, N.; Xie, X. M. *Polymer* **2012**, *53*, 4727−4736.
(16) Ho, R. M.; Chiang, Y. W.; Lin, C. C.; Huang, B. H. *Macromolecules* **2005**, *38*, 4769−4779.
(17) Park, S. C.; Jung, H.; Fukukawa, K. I.; Campos, L. M.; Lee, K.; Shin, K.; Hawker, C. J.; Ha, J. S.; Bang, J. *J. Polym. Sci., Polym. Chem.* **2008**, *46*, 8041−8048.
(18) Torikai, N.; Takabayashi, N.; Noda, I.; Koizumi, S.; Morii, Y.; Matsushita, Y. *Macromolecules* **1997**, *30*, 5698−5703.
(19) Jeong, U.; Ryu, D. Y.; Kho, D. H.; Lee, D. H.; Kim, J. K.; Russell, T. P. *Macromolecules* **2003**, *36*, 3626−3634.
(20) Mayes, A. M.; Russell, T. P.; Satija, S. K.; Majkrzak, C. F. *Macromolecules* **1992**, *25*, 6523−6531.
(21) Shin, K.; Woo, E.; Jeong, Y. G.; Kim, C.; Huh, J.; Kim, K. W. *Macromolecules* **2007**, *40*, 6617−6623.
(22) Woo, E.; Huh, J.; Jeong, Y. G.; Shin, K. *Phys. Rev. Lett.* **2007**, *98*, 136103.

(23) Duran, H.; Steinhart, M.; Butt, H. J.; Floudas, G. *Nano Lett* **2011**, *11*, 1671−1675.
(24) Ferreiro, V.; Douglas, J. F.; Amis, E. J.; Karim, A. *Macromol. Symp.* **2001**, *167*, 73−88.
(25) Li, X.; Hsu, S. L. *J. Polym. Sci., Polym. Phys.* **1984**, *22*, 1331−1342.
(26) Martuscelli, E.; Silvestre, C.; Addonizio, M. L.; Amelino, L. *Makromol. Chem.* **1986**, *187*, 1557−1571.
(27) Mu, D.; Huang, X. R.; Lu, Z. Y.; Sun, C. C. *Chem. Phys.* **2008**, *348*, 122−129.
(28) Okerberg, B. C.; Marand, H. *J. Mater. Sci.* **2007**, *42*, 4521−4529.
(29) Suvorova, A. I.; Hassanova, A. H.; Tujkova, I. S. *Polym. Int.* **2000**, *49*, 1014−1016.
(30) Shi, W. C.; Han, C. C. *Macromolecules* **2012**, *45*, 336−346.
(31) Shi, W. C.; Xie, X. M.; Han, C. C. *Macromolecules* **2012**, *45*, 8336−8346.
(32) Shi, W. C.; Yang, J.; Zhang, Y.; Luo, J.; Liang, Y. R.; Han, C. C. *Macromolecules* **2012**, *45*, 941−950.
(33) Shi, W. C.; Cheng, H.; Chen, F. H.; Liang, Y. R.; Xie, X. M.; Han, C. C. *Macromol. Rapid Commun.* **2011**, *32*, 1886−1890.
(34) Schwahn, D.; Pipich, V.; Richter, D. *Macromolecules* **2012**, *45*, 2035−2049.
(35) Brodeck, M.; Alvarez, F.; Colmenero, J.; Richter, D. *Macromolecules* **2012**, *45*, 536−542.
(36) Ham, S.; Shin, C.; Kim, E.; Ryu, D. Y.; Jeong, U.; Russell, T. P.; Hawker, C. J. *Macromolecules* **2008**, *41*, 6431−6437.
(37) Bang, J.; Jeong, U.; Ryu, D. Y.; Russell, T. P.; Hawker, C. J. *Adv. Mater.* **2009**, *21*, 4769−4792.
(38) Lee, J. K.; Kim, J. S.; Lim, H. J.; Lee, K. H.; Jo, S. M.; Ougizawa, T. *Polymer* **2006**, *47*, 5420−5428.
(39) Huang, P.; Guo, Y.; Quirk, R. P.; Ruan, J. J.; Lotz, B.; Thomas, E. L.; Hsiao, B. S.; Avila-Orta, C. A.; Sics, I.; Cheng, S. Z. D. *Polymer* **2006**, *47*, 5457−5466.
(40) Zhu, L.; Mimnaugh, B. R.; Ge, Q.; Quirk, R. P.; Cheng, S. Z. D.; Thomas, E. L.; Lotz, B.; Hsiao, B. S.; Yeh, F. J.; Liu, L. Z. *Polymer* **2001**, *42*, 9121−9131.
(41) Huang, P.; Zhu, L.; Guo, Y.; Ge, Q.; Jing, A. J.; Chen, W. Y.; Quirk, R. P.; Cheng, S. Z. D.; Thomas, E. L.; Lotz, B.; Hsiao, B. S.; Avila-Orta, C. A.; Sics, I. *Macromolecules* **2004**, *37*, 3689−3698.
(42) Floudas, G.; Tsitsilianis, C. *Macromolecules* **1997**, *30*, 4381−4390.
(43) Hashimoto, T.; Tanaka, H.; Hasegawa, H. *Macromolecules* **1990**, *23*, 4378−4386.
(44) Tanaka, H.; Hasegawa, H.; Hashimoto, T. *Macromolecules* **1991**, *24*, 240−251.
(45) Winey, K. I.; Thomas, E. L.; Fetters, L. J. *Macromolecules* **1991**, *24*, 6182−6188.
(46) Hashimoto, T.; Izumitani, T.; Oono, K. *Macromol. Symp.* **1995**, *98*, 925−949.
(47) Groot, R. D.; Warren, P. B. *J. Chem. Phys.* **1997**, *107*, 4423−4435.
(48) Groot, R. D.; Madden, T. J. *J. Chem. Phys.* **1998**, *108*, 8713−8724.
(49) Qian, H. J.; Lu, Z. Y.; Chen, L. J.; Li, Z. S.; Sun, C. C. *Macromolecules* **2005**, *38*, 1395−1401.
(50) Yan, L. T.; Popp, N.; Ghosh, S. K.; Boeker, A. *ACS Nano* **2010**, *4*, 913−920.
(51) Shillcock, J. C.; Lipowsky, R. *J. Chem. Phys.* **2002**, *117*, 5048−5061.
(52) Horvat, A.; Lyakhova, K. S.; Sevink, G. J. A.; Zvelindovsky, A. V.; Magerle, R. *J. Chem. Phys.* **2004**, *120*, 1117−1126.
(53) Knoll, A.; Magerle, R.; Krausch, G. *J. Chem. Phys.* **2004**, *120*, 1105−1116.
(54) Sriprom, W.; James, M.; Perrier, S.; Neto, C. *Macromolecules* **2009**, *42*, 3138−3146.
(55) Tsarkova, L.; Knoll, A.; Krausch, G.; Magerle, R. *Macromolecules* **2006**, *39*, 3608−3615.
(56) Huang, Y. M.; Xia, H.; Liu, H. L.; Hu, Y. *Macromol. Theory Simul.* **2007**, *16*, 93−100.
(57) Martinez-Veracoechea, F. J.; Escobedo, F. A. *Macromolecules* **2009**, *42*, 1775−1784.
(58) Thompson, R. B.; Ginzburg, V. V.; Matsen, M. W.; Balazs, A. C. *Science* **2001**, *292*, 2469−2472.
(59) Kim, J. U.; O'Shaughnessy, B. *Macromolecules* **2006**, *39*, 413−425.
(60) Nishi, T.; Wang, T. T. *Macromolecules* **1975**, *8*, 909−915.
(61) Nishi, T.; Wang, T. T.; Kwei, T. K. *Macromolecules* **1975**, *8*, 227−234.